Polarization Retention and Switching in Ferroelectric Nano Capacitors with Defects on Tensile Substrates

I. B. Misirlioglu*, M. Yildiz

Faculty of Engineering and Natural Sciences, Sabanci University, Tuzla/Orhanli, 34956 Istanbul, Turkey

Abstract

We analyze the effect of defects on the polarization stability and switching of epitaxial nano capacitor ferroelectric films on tensile substrates using a thermodynamic approach. Defects are either frozen-in dipoles of the *p*-type or trapped space charges. The retention of the in-plane ferroelectric polarization does not suffer nearly at all from the possible presence of dead layers or polar defects but is dramatically impacted by relatively high densities of space charge. Switching is a strong function of defects as well as the presence of a bottom electrode. The out-of-plane dielectric displacement exhibits a spike during switching of the in-plane polarization in films with bottom electrodes but nearly disappears otherwise. Such an effect during polarization reorientation along the film plane could be tailored as a sensing signal. The hysteresis and domain characteristics as a function of interface conditions and defects are discussed for $BaTiO_3$ strained on tensile substrates.

*Corresponding author e-mail: burc@sabanciuniv.edu, Tel: +90 (216) 4839562, Fax: +90 (216) 4839550

Keywords: Ferroelectric thin film devices, domains, hysteresis, thermodynamic modeling

1. Introduction

Long term stability of a switchable ferroelectric polarization (*P)* in epitaxial thin films have been a topic of interest for many research groups as well as the integrated circuit (IC) industry. The designs employing a ferroelectric polarization in a capacitor-type structure have mostly focused on systems with the ferroelectric being sandwiched between two electrodes through which the data or agent signal can both be generated and sensed. It is now well known that ferroelectrics in thin film form sandwiched between two metallic electrodes can suffer from the formation of an utterly non-ferroelectric, insulating layer at the film-electrode interface [1-12] in addition to spatial defect fields such as that of the dislocation type [13-15]. Very recently, the polarity of the interfaces have come to the attention of Wang *et al.* as a possible effective mechanism determining the limit to ferroelectric behavior [16]. Moreover, migration of ionic species under fields emanating from inhomogeneities, especially oxygen vacancies, towards domain-domain and metal-film interfaces contribute to the ferroelectric stability [17-19].

While the sandwich type capacitor (SC) is the most famous the geometry studied, the polarization stability in interdigitated finger electrode type capacitors (IFEC) have attracted some limited attention of a few groups [20-26], including a study on electrode geometry effects [27]. IFECs have mostly been on the agenda for tunable device applications. At a first glance, what appears to be promising for such finger electrode ferroelectric capacitor systems as potential memory elements is that an in-plane P might not suffer from any depolarizing effects originating from the condition that $\nabla \bullet D = 0$ at interfaces with passive layers. Therefore, a switchable P that is minimally impacted by the film-electrode interface conditions might be feasible to tailor. Furthermore, in case of

diffusion of ionic species and vacancies under cyclic applied fields, the potential drops driving such formations along the film plane occur at larger distances, meaning that a longer-lasting benefit from the ferroelectric *P* might be realized. Despite all these, remanence of *P* and the transition characteristics of FE films with interdigitated finger electrodes remains as a topic studied in a very limited number of works.

In this article, we study the electrical properties of [001] $BaTiO_3$ (BT) grown on epitaxially tensile perovskite type [001] single crystal substrates (TSC) to quantitatively study the effect of IFEC electrostatic boundary conditions on *P* configurations. Compressive substrates for BT usually favors an out-of-plane *P* while TSC induces an in-plane *P* owing to the tensile misfit with BT. Employing the Landau-Ginzburg-Devonshire (LGD) functional in a two dimensional frame, we compare and contrast on the differences of properties for the two capacitor geometries with dead layers at the film-electrode interfaces. We find that frozen-in defect complexes due to ionic vacancies do not so profoundly alter the IFEC films in contrast to SC type capacitors. Moreover, we also find that the BT films in the IFECs exhibit a “spike” of dielectric displacement at the exposed surface between the electrodes and that this behavior is a very strong function of whether a bottom electrode is present or not. The presence of such an effect can be tailored as an effective means to sense in-plane *P* switching.

2. Theory and Methodology

The schematic of the capacitor geometry considered is given in Figure 1. A two dimensional grid is constructed that has 400*n* x *kn* cells where *k* (400) is the number of cells along the film thickness (width) and each cell, *n*, has a dimension of 0.4 nm, nearly

the lattice parameters of well known pseudocubic perovskites such as BT to imitate the order of lengths at which P can vary.

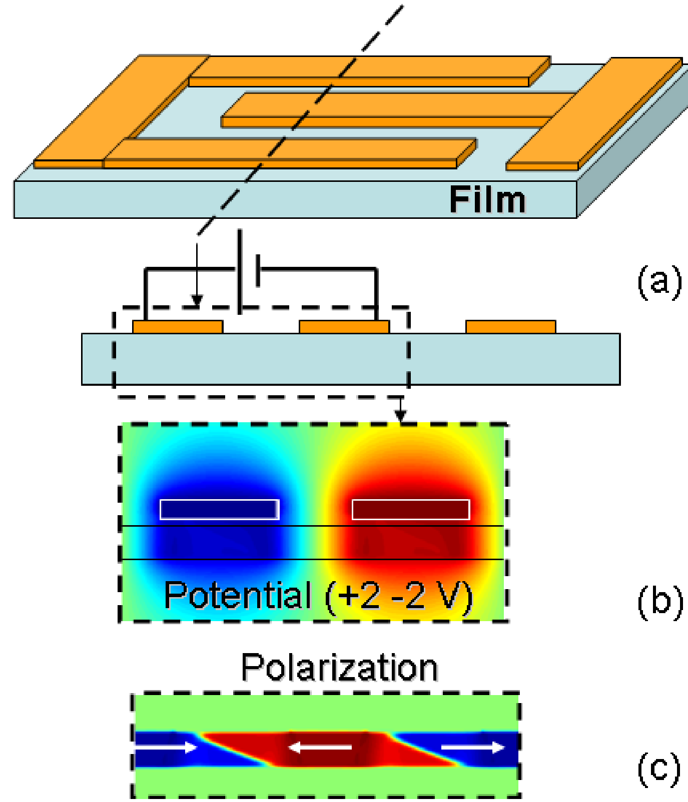

Figure 1. (Color online) (a) A schematic of the finger electrode capacitor. The potential in (b) and the in-plane polarization components in (c) are shown for demonstration of the computational domain.

P is obtained by solving the equations of state derived from the LGD free energy for an epitaxial monodomain (001) ferroelectric film on a (001) cubic substrate coupled with the Maxwell equation for dielectric displacement employing a finite difference discretization. The total volumetric free energy of the ferroelectric thin film capacitor system is:

$$F_T = \int_V \left[w(F_0 + F_P + F_E + F_G - F_{ES}) + (1-w)F_{DL} \right] dV \qquad (1)$$

where w is a step-wise function defining the interface between the dead layer and the ferroelectric: w=1 when $-h/2 \leq z \leq +h/2$ *and* w=0 when $-h/2-s < z < -h/2$ and $+h/2 < z < s+h/2$, s is the dead layer thickness (one unit cell in this work when present, zero when absent), h is the thickness of the ferroelectric layer. The electrode-dead layer interfaces are at $-h/2-s$ and $s+h/2$ respectively. F_0 is the energy of the paraelectric state and is taken as zero due to the absence of order-parameter related terms. F_P is the energy due to the presence of P and is given by

$$\begin{aligned} F_P &= \alpha_1(P_1^2+P_2^2+P_3^2)+\alpha_{11}(P_1^4+P_2^4+P_3^4)+\alpha_{12}(P_1^2P_2^2+P_1^2P_3^2+P_2^2P_3^2) \\ &\quad +\alpha_{111}(P_1^6+P_2^6+P_3^6)+\alpha_{112}[P_1^4(P_2^2+P_3^2)+P_2^4(P_1^2+P_3^2)+P_z^4(P_1^2+P_2^2)] \\ &\quad +\alpha_{123}P_1^2P_2^2P_3^2 \end{aligned} \quad (2)$$

where P_i (i=1,2,3) are the components of P in the ferroelectric state, and α_i, α_{ij}, and α_{ijk} are the dielectric stiffness coefficients. F_E in Eq. (1) is the internal elastic energy both due to the misfit between the film and the substrate, ε_{ij} as well as the self-strain in the ferroelectric state, ε_{ij}^0, given by:

$$F_E = \frac{1}{2}C_{ijkl}\left(\varepsilon_{ij}-\varepsilon_{ij}^0\right)\left(\varepsilon_{kl}-\varepsilon_{kl}^0\right) \quad (3)$$

where the C_{ijkl} are the elastic stiffnesses for a cubic crystal. ε_{ij}^0 is the transformation strain due to the paraelectric-ferroelectric phase transition in the film and is given by:

$$\varepsilon_{ij}^0 = Q_{ijk}P_k \quad (4)$$

with Q_{ijk} being the electrostrictive coefficient tensor for a cubic crystal. The shear components of misfit stress in (3) are taken as zero due to the traction-free film surface. The in-plane biaxial misfit state with equal orthogonal components $\varepsilon_{11} = \varepsilon_{22}$, due to

epitaxy require that $P_1 = P_2$, and the rest of the equations are given hereafter accordingly. The gradient energy in Eq. (1) we employ is:

$$F_G = G_{33}\left(\frac{dP_3}{dz}\right)^2 + G_{31}\left(\frac{dP_3}{dx}\right)^2 + G_{13}\left(\frac{dP_1}{dz}\right)^2 + G_{11}\left(\frac{dP_1}{dx}\right)^2 + G_{23}\left(\frac{dP_2}{dz}\right)^2 + G_{21}\left(\frac{dP_2}{dx}\right)^2 \tag{5}$$

where G_{ij} are the gradient energy coefficients. For the sake of convenience, we shall assume that the gradient energy coefficient is isotropic, $G_{33} = G_{31} = G_{13} = G_{11} = G_{23} = G_{21} = G$. F_{ES} is the electrostatic energy of the system that is a function of the electrostatic boundary conditions of the capacitors as well as gradients of P and can simply be written as:

$$F_{ES} = -(E_x P_1 + E_z P_3) \tag{6}$$

for $w = 1$ where E_x and E_z are the in-plane and out-of-plane components of the electric field respectively. F_{DL} is simply the energy of the dead layer that is assumed to be a linear dielectric and is given by (for $w = 0$):

$$F_{DL} = \varepsilon_0 \varepsilon_r (E_x^2 + E_z^2) \tag{7}$$

where ε_r is the dielectric constant of the dead layer and is assumed to be isotropic for convenience. Minimization of Eqn. (1) for w=1 yields the Euler-Lagrange relations as:

$$\frac{dF_T}{dP_3} - \frac{d}{dz}\left(\frac{dF_T}{df_1}\right) - \frac{d}{dx}\left(\frac{dF_T}{df_2}\right) = 0, \quad \frac{dF_T}{dP_1} - \frac{d}{dz}\left(\frac{dF_T}{df_3}\right) - \frac{d}{dx}\left(\frac{dF_T}{df_4}\right) = 0 \tag{8}$$

with $f_1 = dP_3 / dz$, $f_2 = dP_3 / dx$, $f_3 = dP_1 / dz$ and $f_4 = dP_1 / dx$. From Eqns.(8) and (1), the equations of state for the ferroelectric layer are written as:

$$G\left(\frac{d^2P_3}{dz^2}+\frac{d^2P_3}{dx^2}\right)=2\alpha_3^m P_3+4\alpha_{13}^m P_3\,P_1^2+4\alpha_{33}^m P_3^3+6\alpha_{111}P_3^5$$
$$+\alpha_{112}(4P_3P_1^4+8P_3^3P_1^2)+2\alpha_{123}P_3P_1^4-E_Z(x,z)$$

(9a)

$$G\left(\frac{d^2P_1}{dz^2}+\frac{d^2P_1}{dx^2}\right)=2\alpha_1^m P_1+2(2\alpha_{11}^m+\alpha_{12}^m)P_1^3+2\alpha_{13}^m P_1P_3^2+6\alpha_{111}P_1^5$$
$$+2\alpha_{112}[3P_1^5+3P_1^3P_3^2+P_1P_3^4]+2\alpha_{123}P_1^3P_3^2-E_X(x,z)$$

(9b)

in the ferroelectric film $(w=1)$ where the α_3^m, α_{13}^m, α_{33}^m are the renormalized dielectric stiffness coefficients, modified by the misfit strain and the two-dimensional clamping of the film [28]. The dead layer, when present, is assumed to be a high-k dielectric whose dielectric constant, ε_r, is 20 to exemplify its effects. The electric fields in both the ferroelectric layer and the dead layer are computed from the gradient of the electrostatic potential ϕ,

$$E_Z=-\frac{d\phi}{dz},\ E_x=-\frac{d\phi}{dx} \tag{10}$$

Note that ϕ contains all contributions from boundaries, defects and charge distributions when present and is solved at each point in the system as a function of P components from the Maxwell relation $divD=\rho$ that can explicitly be written as,

$$\frac{d^2\phi}{dz^2}+\frac{d^2\phi}{dx^2}=\frac{1}{\varepsilon_b\varepsilon_0}\left(\frac{dP_z}{dz}+\frac{dP_x}{dx}-\rho\right) \tag{11a}$$

in the ferroelectric layer and

$$\frac{d^2\phi}{dz^2}+\frac{d^2\phi}{dx^2}=\frac{\rho}{\varepsilon_r\varepsilon_0} \tag{11b}$$

in the dead layer where ρ is the volumetric charge density (0 when no impurities are present) with ε_b being the background dielectric constant of the ferroelectric (taken as 10 in this work). The boundary conditions we employed for $P_{1,3}$ are

$$\left[P_1 + \lambda \frac{dP_1}{dz}\right]_{z=-\frac{h}{2}-s,\frac{h}{2}+s} = 0, \left[P_3 + \lambda \frac{dP_3}{dz}\right]_{z=-\frac{h}{2}-s,\frac{h}{2}+s} = 0 \qquad (12)$$

at the top and bottom electrode-film interface of the ferroelectric where the extrapolation length, λ, is taken as infinite. Periodic boundary conditions are used along the *x*-axis, i. e., $P_3(z, x=0) = P_3(z, x=L)$, $P_1(z, x=0) = P_1(z, x=L)$. We apply Dirichlet boundary conditions to solve the electrostatic potential. At the dead layer-electrode interfaces *-h/2-s* and *s+h/2*, $\phi = 0$ correspond to total charge compensation while periodic boundaries are adopted along *x* as given above. ϕ is given for the two electrodes as exemplified in Figure 1b. The free surfaces in the IFEC capacitor has to satisfy Eqn. (11) and periodic boundaries are employed along *x*. The effect of a bottom electrode in the IFEC system is considered via assigning $\phi = 0$ @*z=-h/2-s* when specified.

Equations (9) – (12) are solved simultaneously employing a Gauss-Seidel iterative scheme subject to boundary conditions mentioned above and (11) and (12) for *P*. We limit ourselves to 5000 iterations converging to a difference of about 10^{-8} between consecutive iterative *P* solutions when ferroelectricity exists. The defects, when present, are assumed to be frozen-in polar complexes in the lattice with the restriction that they cannot be too close to each other in order to test long-range effects or they are space charges due to ionized impurities ($\rho \neq 0$). For the former case, their presence is introduced via fixing the relevant *P* components at a randomly chosen cell, creating local frozen-in dipoles. Thus the impact of the frozen-in type defects is two fold: They can pin

local P via the gradients in P they create and these gradients also produce a spatially varying potential via Eqn. 11a under given boundary conditions. Thus $E_{x,z}(x,z)$ in Eqn. 9a and 9b contains the defect fields, too, via the spatial gradients of the potential computed from Eqn. 10 with the boundary conditions for P and ϕ in the system.

As prescribed above, the frozen-in dipole defect positions are fixed with respect to the bottom electrode/free surface coordinates. Thus, their positions are automatically altered when film thickness changes. This mostly impacts the symmetry of the defect positions with respect to the midsection of the film for ultrathin films but is still good enough to demonstrate their effects in ultrathin structures We also must add here that, within the 2D limit of the study, our results for IFECs with defects might not be exactly representing the behavior of 3D systems with very few defects due to variation in the averaging of properties. On the other hand, they can be compared to 3D systems with relatively high density of defects where averaging over the volume will be close to the averaging over a 2D slice of the system considered here.

To get the electric field dependent behavior of the films, we simply change ϕ on the left electrode, assigning the other $-\phi$. A triangular signal for ϕ is used to get the hystereses of the films with maximum voltage drop amplitude being 4V. The signal consists of 100 steps between -2V and +2V and each electrode attains the opposite sign of the other. Note that the fields will be highly inhomogeneous in the IFEC. At every incremental bias step, we allow the films to reach their near-equilibrium P configuration. Hence, the hystereses in our simulations are in the quasi static limit. The electrode thicknesses are 8 nm and due to the free surfaces exposed between the top electrodes, we solve the ϕ outside the IFEC films, too. The section exposed between the array of finger

electrodes is 32 nm. These IFEC films also experience fields between the finger electrodes and a grounded bottom electrode when there is one. Figure 1b-c is an example to demonstrate the characteristic distribution of potential and the P_x under 2V bias between the finger electrodes.

We considered in this study the heteroepitaxial (001) BT films fully strained on a non-ferroelectric (001) hyphothetical cubic perovskite substrates inducing a 1% tensile misfit with interdigitated metallic finger electrodes (IFEC). We assumed this hypothetical substrate for demonstrative purposes. However, the approach presented here can easily be adapted to any pseudocubic ferroelectric perovskite film. The values of the dielectric stiffness coefficients and other thermodynamic parameters of BT entering the calculations are taken from Ref. 22. Simulation results are presented for films of 8 nm, 16 nm thickness at room temperature (T=25°C).

3. Results and Discussion

Here we discuss the results for the ferroelectric IFEC films at RT, under a fixed applied bias as well as a triangular signal. We consider dipolar defects whose schematic is given in Figure 2: A frozen-in, dipole couple or so-called *p*-type complex formed due to a missing O vacancy where the B-site ions are shifted into opposite corners in the two neighboring unitcells to reduce repulsive forces under fully ionic consideration. The variants of this type of defect in this work is chosen randomly and therefore the defect dipole moment can point along any of the 2 axes given in Figure 2.

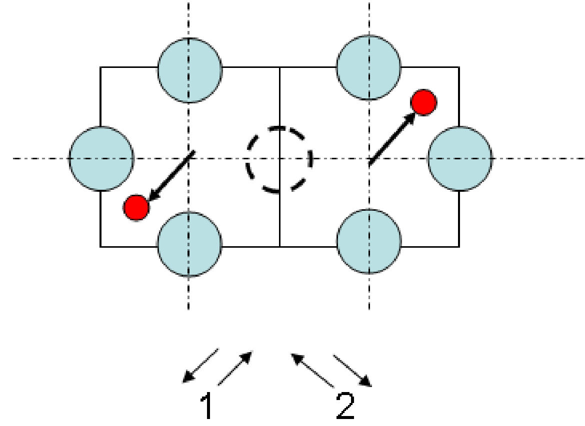

Figure 2. (Color online) The *p*-type defects in this study. The dashed circle in the middle denotes the missing oxygen ion while the red atoms denote the Ti ions. The arrows indicate the shift of the positively charged Ti ions, forming a antiparallel configured dipole couple of not-ferroelectric origin. 1 and 2 denote the possible configurations considered in this work.

Such a defect constitutes a so-called *p*-type defect [29] and is similar to the defect type whose mechanism of formation was reported in Ref. 30 accompanied by relaxation of the atomic forces.

Due to the different variations in electrostatic potential around the types of defects menitoned above, they might be expected to have a quite complicated impact on the properties of IFEC films. Atomistic first principles studies have reported substantially high dipole moments for vacancy-induced dipoles, comparable to or more than the moments of spontaneous ferroelectric dipoles [31]. Keeping in mind the results of these studies, we consider highly stable defect-dipole sites whose values are assigned as 0.25 $C.m/m^3$, close to the bulk $BaTiO_3$ P at RT. In section 3.2., we also give our results for domain structures of P in IFEC films in the presence of homogeneous space charge

distribution as the trends for remanence we observed are quite different than polar defects.

3.2. Ferroelectricity at Room Temperature in IFEC Thin Film Capacitors

Using exactly the same method described in Section 2 with the appropriate BCs, we provide our RT results for the IFEC films in this section. During the simulations of the domain states in the IFEC films, we note that the presence or absence of a dead layer (s=0 or s=1 respectively) has no significant impact on the domain morphologies of the 8 nm and 16 nm thick IFEC films with or without defects. Therefore we give in this section our results for s=1 to avoid repetition of similar plots and evaluation. We emphasize here the states under bias (sufficient to saturate the P_x in the plane of the film) followed by removal of the bias. The latter is to display the domain configuration under remanence. We consider IFEC films only with top finger electrodes throughout the discussion. For the RT results herein presented, the presence of a bottom electrode also has no apparent influence on the P configuration near saturation bias followed by zero bias. The effect of a bottom electrode, however, becomes a very important parameter for switching where related details are discussed in Section 3.4.

Solution of the P_x and P_z starting from fluctuations around zero under 1% tensile misfit at zero bias develop into a single domain state of remanent P_x pointing in either $-x$ or $+x$ direction with zero P_z and these are not given here for brevity. Applying 1.5V and -1.5V bias on the electrodes respectively, we show in Figure 3a-c the in-plane domain state stability of P_x in the 8 and 16 nm thick defect-free films. The resultant configuration is the consequence of the inhomogeneous distribution of the field inside the film. Field

distribution in finger electrode capacitors have been often approximated as a constant in-plane field, which is a very unrealistic assumption that would prevent correct evaluation of such systems. In agreement with our conclusions, Ref. 25 shows that this highly inhomogeneous distribution even in larger real systems lead to different retention and fatigue behavior of in-plane P in different regions with respect to the electrode positions. Likewise, in this study, removal of the bias leads to an apparently stable remanence of P_x that changes sign along x both in the 8 nm and 16 nm thick films as displayed in Figure 3b-d.

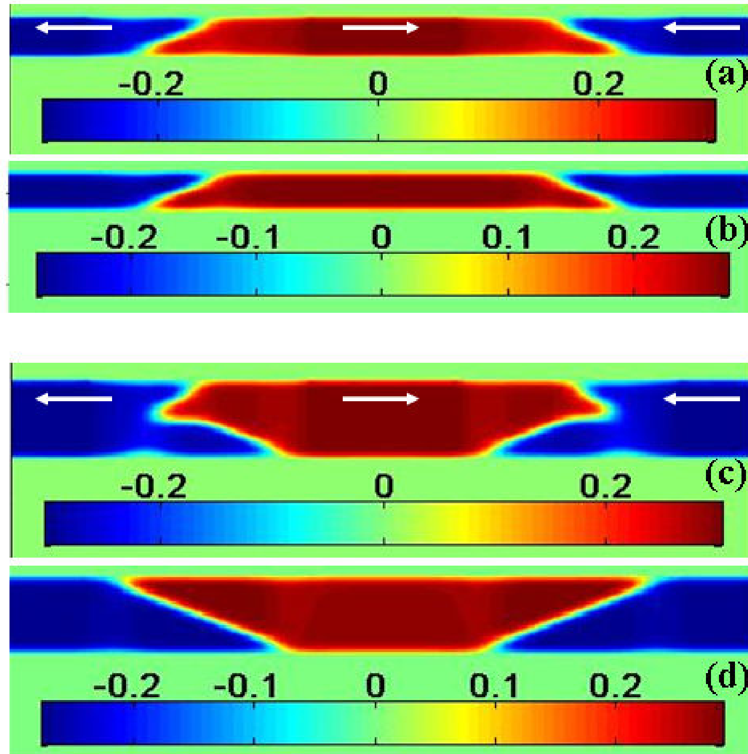

Figure 3. (Color online) Map of P_x in (a) 8 nm thick defect-free IFEC film under bias, (b) 8 nm thick defect-free IFEC film after bias removed, (c) 16 nm thick defect-free IFEC film under bias, (d) 16 nm thick defect-free IFEC film after bias removed.

Due to the condition of the remanent P being parallel to the interface, there is no jump in dielectric displacement at neither $z=h/2$ or $z=-h/2$, hence no depolarizing fields along x when external bias is zero. Therefore the 8 nm and 16 nm IFEC films do not suffer much from thickness effects compared to the SC ones. P_z has small but finite values at zero bias near the domain boundaries but attains spatially varying solutions at the order of P_x under bias due to the potential drops from the finger electrodes towards bottom of the film.

3.2.1. p-type Defects Present

When the aforementioned type of defects are present with $s=1$, the above picture for the 8 nm film only slightly changes. Turning our attention to Figure 4a-b for the 8 nm IFEC films with *p*-type defects, we see no induction of any type of nano-sized domains. Upon removal of the bias, the P_x configuration does not change much and more or less sustains its state in the biased case for *p*-type defects (Figure 4b). The domain boundaries between the P_x components pointing along $-x$ and $+x$ directions undergoes a slight or even negligible rearrangement. P_z, after removal of the bias, is zero except components forming due to slight rotations of P near the interfaces where P_x changes sign.

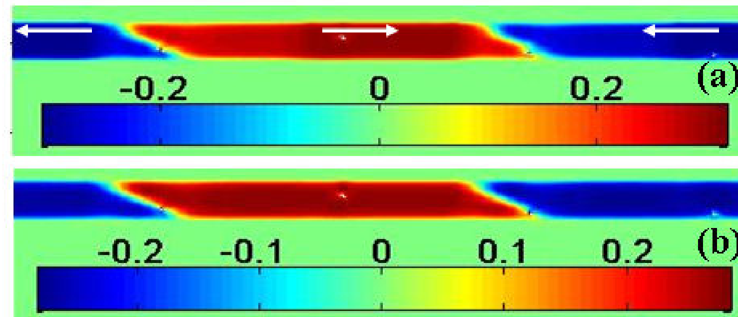

Figure 4. (Color online) Map of P_x in (a) 8 nm thick IFEC film with *p*-type defects under bias, (b) 8 nm thick IFEC film with *p*-type defects after bias removed.

Therefore, we observe from Figure 4 that, even in the presence of dipolar defects, there is hardly any loss of the spatial state in between the electrodes attained under bias. The common observation in the simulations of the IFEC films here is that defects act as local perturbation centers to the order state and do not trigger domain formation. However, these RT results obviously do not imply that the hystereses and phase transition characteristics for the defected and defect-free 8 nm thick IFEC films will also be similar.

Looking at the response of the 16 nm IFEC film with *p*-type defects given in Figure 5, we again see that the configuration of P_x under bias (Figure 5a) and zero bias (Figure 5b) are similar, with the exception of the interface asymmetry with respect to the midpoint of the structure in the 16 nm IFEC with *p*-type defects. The same configurational trend of P_x distribution as in the 8 nm IFEC film is observed but a larger switched volume is present in 16 nm film. Stability of P_x under applied bias and upon removal of the bias in the IFEC films with defects is only slightly altered.

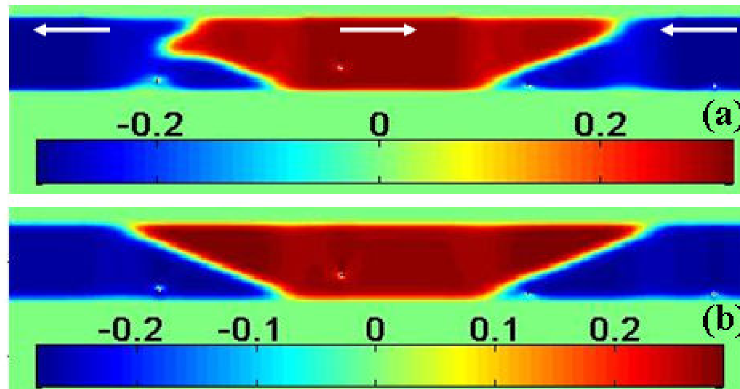

Figure 5. (Color online) Map of P_x in (a) 16 nm thick IFEC film with *p*-type defects under bias, (b) 16 nm thick IFEC film with *p*-type defects after bias removed.

If examined carefully via Figure 4 and Figure 5, the defects near the bottom interface of the 16 nm film are more visible under zero bias and appear to have a larger area of

influence in contrast to the 8 nm thick one. This is because of the decay of the magnitude of the electric field into the film volume away from the finger electrodes and that the "defect configured P_x" becomes more prominent around defects compared to applied field effects in the 16 nm film. Regions in the vicinity of the electrodes are naturally under a stronger influence of the applied bias and this overrides the effects due to dipolar defects as in the 8 nm thick film. But again it should be borne in mind that the stabilities of the P_x components shown in the colormap plots do not reveal how the hystereses would be impacted by these defects.

Overall, the P_x component in the IFEC films under tensile in-plane misfit strains appear to be stable without any electrical domain complications similar to that of observed in the SC films. The remanence mentioned for the IFEC geometry, on the other hand, is the stability of a switchable but a local P_x with respect to the electrode positions and widths. The electrostatics fields of the *p*-type defects is also more complicated as there is an abrupt sign change of P_x and P_z at the sites neighboring defected cells. But we did not observe any dramatic variations in the domain configurations of IFEC films with *p*-type defects.

3.2.2. Space Charge Formation Present

Continuous distribution of space charge due to relatively large densities of carriers trapped at deep states have been mostly analyzed in SC type ferroelectrics and superlattices [32-39]. Such formations can also have a significant impact on the remanence of the P_x in IFEC capacitors. We give our results here for a constant density and an asymmetrically distributed density of space charge under bias and after removal of bias

with no bottom electrode present. Figure 6a-d displays the state of P_x under total 4V bias followed by removal of this bias for the 16 nm and 8 nm thick IFEC films respectively. A continuous distribution of space charge at constant density of 10^{24} C/m^3 does not have an apparent effect on P_x in both the 16 nm thick IFEC film when under bias and when no bias exists and is skipped here. Such a charge distribution normally produces an electric field in a slab that is zero in the middle and is symmetrical with respect to the mid-section of the film thickness. However, one should pay attention that, in the case of finger electrodes, this situation becomes quite different owing to boundary conditions. When looking at Figure 6a-b, a homogeneous ρ of 10^{26}, on the other hand, significantly interferes with the applied field and there is no single domain remanence in the region between the electrodes upon removal of the applied in-plane bias.

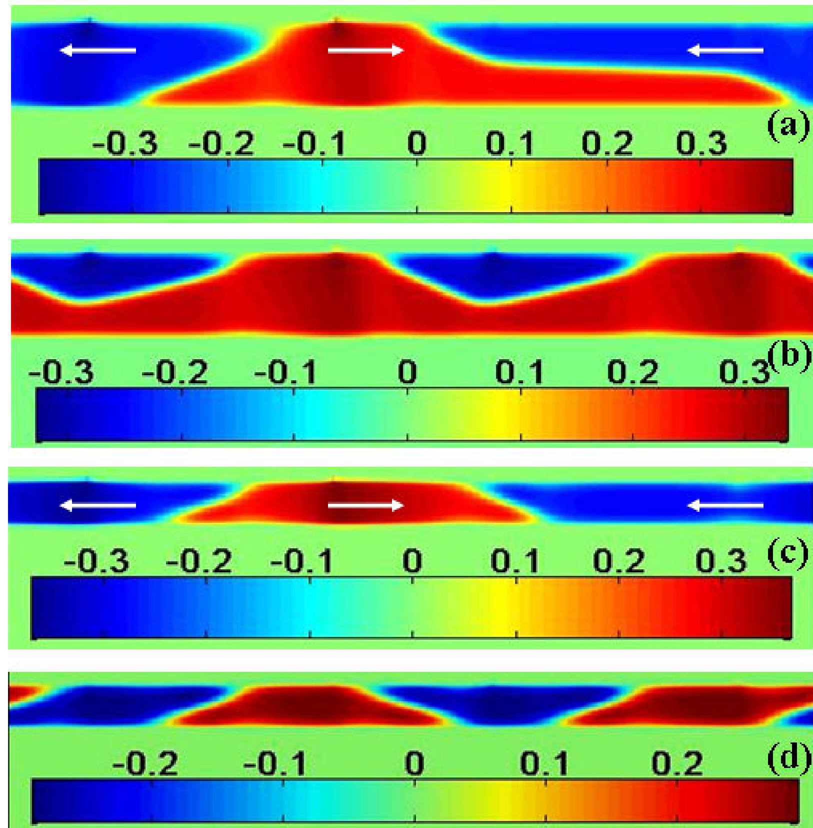

Figure 6. (Color online) Map of P_x in (a) 16 nm thick IFEC film with homogeneous space charge density of 10^{26} C/m^3 under 4V bias and (b) after bias removed, (c) P_x in 8 nm thick IFEC film with homogeneous space charge density of 10^{26} C/m^3 under bias and (d) after bias removed.

A homogeneous space charge density of 10^{24} C/m^3 does not influence the stability of the P_x in the 8 nm thick IFEC both in the presence and absence of applied, the system retains its "under-bias P_x" state and is not given here for brevity. Raising this value to 10^{26} C/m^3, however, alters P_x and P_z dramatically where a periodic domain structure in P_x that is smaller than the electrode periodicity is obtained upon removal of bias as provided in Figure 6c-d. We also note that the switched fraction under applied bias in the 8 nm IFEC film is much smaller in relative volume than the charge-free 8 nm thick IFEC already given in Figure 3a. Upon removal of applied bias, these volumetric charge dictates the state of P_x and the configuration induced under bias is totally destroyed (Figure 6c-d).

3.4. Characteristics of the Hysteresis Loops in IFEC Films

3.4.1. No defects

Applying the triangular bias signal as explained in section 2, we extracted the hysteresis loops of the IFEC films for P_x. As already mentioned, the field distribution in this geometry is not uniform along the film volume and that parts of the films switch in opposite directions. The region between the electrodes are tracked to probe the P_x and P_z as a function of applied bias signal because the average P_x of the entire film does not

yield a hystereses due to the inhomogeneous nature of the field distribution in the given electrode positions. Noting that the presence or absence of a dead layer does not make a difference in the IFEC geometry, we studied this system for s=1. The very reason for this is that there is no remanent P component in the dielectric displacement normal to the electrode-film interface. We computed the average dielectric displacement at the surface exposed between the top finger electrodes to identify whether a signal here is possible to tailor during switching of P_x.

Figure 7a-b displays the hysteresis loop in the 8 nm and 16 nm thick IFEC films in both the presence and absence of a bottom electrode where P_x in the middle of the region between the electrodes was tracked. In the absence of defects, there is nearly identical square hystereses in both IFEC films. Also in Figure 7, the impact of the presence of a bottom electrode in the IFEC films is clear: Both the 8 nm and 16 nm films switch at a lower coercive field in the thermodynamic limit. Moreover, films without the bottom electrodes have a displaced hysteresis towards the positive bias, indicating it is more difficult for P_x to switch from $-x$ to $+x$ direction in the middle region between the electrodes. This difference in the switching behavior in the IFEC films with bottom electrodes is due to the presence of a large out-of-plane electric field formation that stabilizes an induced P_z coupling to P_x via the cross terms in the LGD energy. Right at the coercive bias of P_x we find relatively large values for the solution of P_z, and nearly zero elsewhere in the bias range of interest. Therefore the film with the bottom electrode passes through an "easy induced" monoclinic state during switching favored by the field along z axis which seems to reduce the coercive field value for P_x.

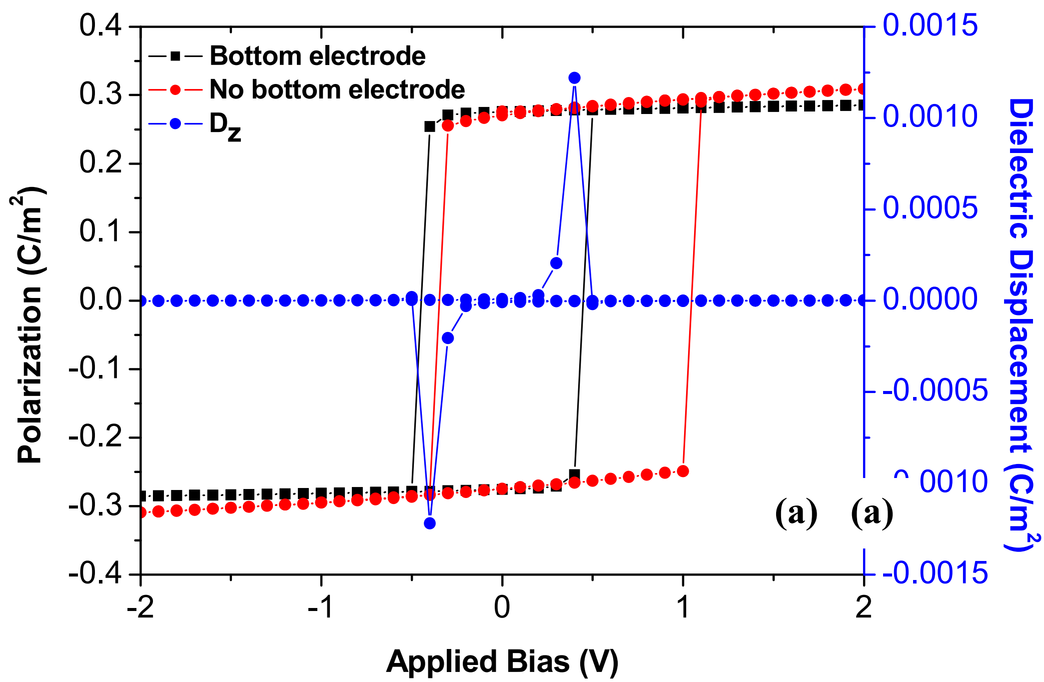

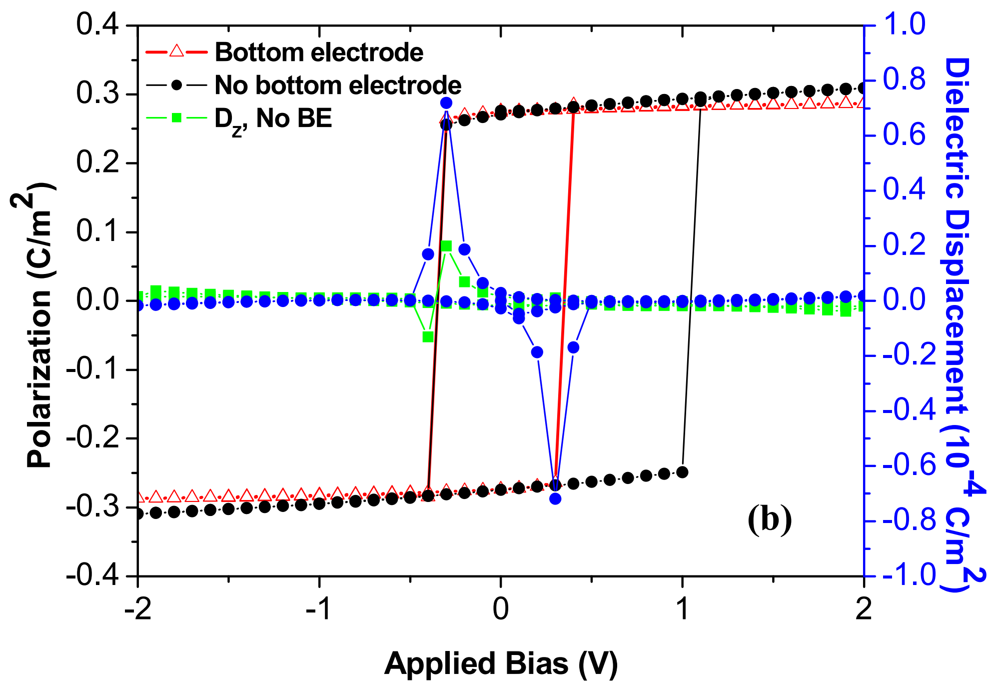

Figure 7. (Color online) Hysteresis loops and dielectric displacement along *z* (right axis) for defect-free (a) 8 nm thick IFEC film and (b) 16 nm thick IFEC film. 'BE' (b) stands

for ‘bottom electrode’ and the green curve is provided to display the dielectric displacement at the surface between the electrodes when there is no bottom electrode.

The thickness dependent effects in IFEC films with dead layers do not have an as profound an effect on remanent P stability as in SC films. Moreover, this “nearly dead-layer independence of polarization” of IFEC films is a very important and advantageous aspect in device design. We find that $\langle D_z \rangle$ on the exposed surface between the top-electrodes, especially in the presence of a bottom electrode, undergoes abrupt variations near the coercive bias values of P_x. These peak-like abrupt variations in D_z could be useful as a sensing signal of the switching for instance, via tracking the change of dielectric displacement along z near the bottom electrode or an electrode placed in between the top ones. One important finding is that the sign of these peaks are thickness dependent and, in the absence of the bottom electrode, such peaks nearly disappear and become very weak or negligible. This is because of the depolarizing fields taking effect that oppose P_z during the switching of the P_x and thus no clear peak-like P_z variations are observed. Therefore, the ease with which P_z switches also impacts the switching characteristics of P_x as demonstrated.

3.4.2. p-type Defects Present

We now discuss the effect of p-type type defects on the 8 nm and 16 nm thick IFEC films for s=1. In this section, we again skip the discussion of the characteristics of the hystereses for s=0 because whether s=0 or s=1 has only a negligible effect on the behavior of P_x in the IFEC films. Owing to the highly inhomogeneous fields during

hystereses extraction tracking the P_x in the middle section of the film is what we pursue again in order to justify defect related effects. P_x in the central region between the electrodes is influenced by their existence, even if several tens of nanometers away from defect sites implying the long-range effects of frozen-in dipole complexes. We next discuss the alterations in the hysteresis loops in the 8 nm and 16 nm films with defects.

The presence of *p*-type defects have a substantial influence on the hystereses of both the 8 nm and 16 nm thick films as seen in Figure 8a-b. In the presence of bottom electrodes, there is a visible shift of the hysteresis loops with a slight increase in the coercive bias values. One would normally expect this shift to be at a minimum due to the relatively symmetric potentials created around the dipole couple. However, the position of the defects with respect to the electrodes and their assigned values already do create a highly asymmetrical distribution of the fields. Moreover, this shift will also depend on the region where the local P_x value is probed. Thus, we give here the general characteristics and trends to avoid a lengthy discussion on this aspect.

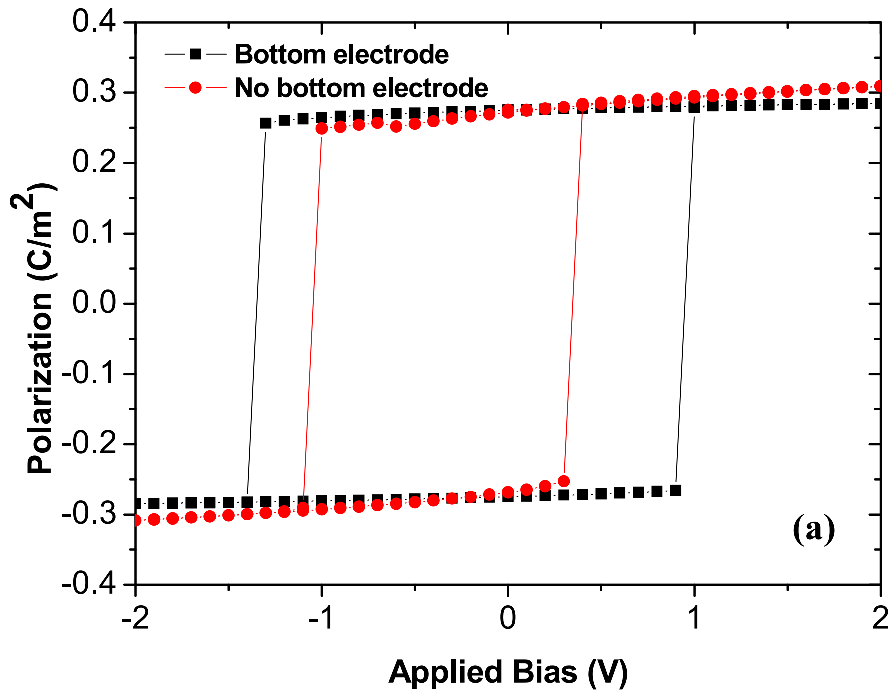
Bottom electrode
No bottom electrode
Polarization (C/m2)
Applied Bias (V)
(a)
0.4
0.3
0.2
0.1
0.0
-0.1
-0.2
-0.3
-0.4
-2
-1
0
1
2

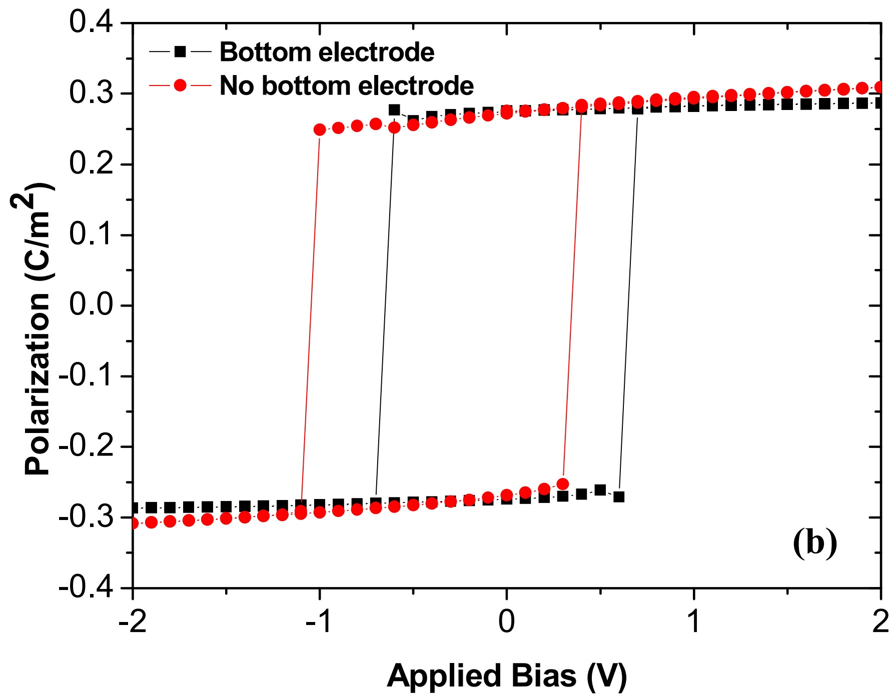
Bottom electrode
No bottom electrode
Polarization (C/m2)
Applied Bias (V)
(b)
0.4
0.3
0.2
0.1
0.0
-0.1
-0.2
-0.3
-0.4
-2
-1
0
1
2

Figure 8. (Color online) Hysteresis loops and displacement along z (right axis) for (a) 8 nm thick IFEC film and (b) 16 nm thick IFEC film with polar p-type defects.

While the loops in the 16 nm IFEC film are displaced along the bias axis with p-type defects (Figure 8b), a swelling of these loops accompanies the shifts in the 8 nm film regardless of the presence of bottom electrode (Figure 8a). One must remember that the P_x component in the middle of the film is not under the influence of any strong depolarizing or internal bias fields originating from asymmetric boundaries. We note that due to the components of the p-type defect dipoles along $+x$ and $–x$, the coercive field increases in both signs of the bias axis due to local pinning. In addition, the fields along z-axis emanating from any inhomogeneity in D_z in the 8 nm IFEC film are expected to be stronger than in the 16 nm one for the obvious reason: Steeper decay of potentials in the 8 nm film compared to the 16 nm film. The thinner IFEC is more sensitive to p-type defects as the switching bias for the perfect 8 nm and 16 nm thick IFEC structures are nearly the same regardless of the absence or presence of a bottom electrode (Figure 7).

Overall, despite the complicated nature of the defect effects in the highly inhomogeneous field distribution of the IFEC films, we can make some remarks to a certain extent regarding the hystereses characteristics: Figure 8a clearly reveals that the 8 nm IFEC films with defects require higher bias fields to switch P in between the electrodes. The bottom electrode strongly alters the switching characteristics of the system and the way in which the loops shift are relatively different in the 8 nm and 16 nm thick IFEC films. The 8 nm thick IFEC system suffers more profoundly from pinning due to defects. A striking characteristic, however, to note in both the 8 nm and 16 nm IFEC

films is that there is nearly no deformation of loops and they preserve the squareness. The absence of a bottom electrode apparently eradicates easy switching in the 16 nm film with defects but no such conclusion can be arrived at for the 8 nm thick IFEC film. With efficient IC architecture, IFECs might be a feasible option to tailor owing to the nearly defect insensitive nature of the P_x remanence.

4. Conclusions

In this study, we showed that due to the configuration of P in IFEC type capacitors, the sensitivity of these systems to electrostatic BCs is dramatically less than SC type. The IFEC switching is impacted by the presence or absence of a bottom electrode, implying the coupling of P_x to induced P_z near switching. Our simulations indicate that D_z makes a sharp anomaly at the coercive field of the P_x and can be used as a signal to sense switching. This signal, however, nearly disappears when a bottom electrode is not present and concomitantly thermodynamic coercive fields for P_x increases.

The presence of *p*-type polar in IFEC films induces a shift in the loops along the bias axis, accompanied by an increase in the coercive fields for ultrathin structures. The overall effect of frozen-in dipolar *p*-type defects is that the steep gradients around the defect sites that decay towards the electrodes create strongly inhomogeneous fields. These fields, in the case of the SC type films, strongly couple to P_z , a well understood and natural outcome, while the coupling of these fields in the IFEC geometry to P_x is weaker. The polar defects in thin IFEC films increase the coercive bias in the thermodynamic limit due to spatial pinning but no loss of remanency due to electrical

domain formation following removal of the bias is observed. A contiuous distribution of space charge when relatively high in density, on the other hand, destroys any remanence in IFEC structures after removal of bias and nearly no hystereses is expected, a profound difference compared to the effect of polar defects. The impact of space charges on phase transition and retention characteristics of ultrathin structures, in our view, deserve separate attention and will be given in another study.

References

1. M. Dawber, K. M. Rabe, and J. F. Scott, Rev. Mod. Phys. **77**, 1083 (2005).
2. R. R. Mehta, B. D. Silverman, and J. T. Jacobs, J. Appl. Phys. **44**, 3379 (1973).
3. A. M. Bratkovsky and A. P. Levanyuk, Phys. Rev. Lett. **84**, 3177 (2000).
4. T. M. Shaw, S. Troiler-McKinstry, P. C, Mcintyre, Ann. Rev. Mat. Sci. **30**, 263 (2000).
5. J. Junquero and P. Ghosez, Nature **422**, 506 (2003).
6. G. Gerra, A. K. Tagantsev, N. Setter, and K. Parlinski, Phys. Rev. Lett. **96**, 107603 (2006).
7. G. Gerra, A. K. Tagantsev, N. Setter, Phys. Rev. Lett. **98**, 207601 (2007).
8. Massimiliano Stengel, Nicola A. Spaldin, Nature Lett. **443**, 679 (2006).
9. Y. Yacoby, Y. Girshberg, E. A. Stern and R. Clarke, Phys. Rev. B **74**, 104113 (2006).
10. S. Prosandeev and L. Bellaiche, Phys. Rev. B **75**, 172109 (2007).
11. Zhou, C., Newns, D. M. J. Appl. Phys. **82**, 3081 (1997).
12. R. Ahluwalia and D. J. Srolovitz, Phys. Rev. B **76**, 174121 (2007).

13. S. Y. Hu, Y. L. Li and L. Q. Chen, J. Appl. Phys. 94, 2542 (2003).
14. V. Nagarajan, C. L. Jia, H. Kohlstedt, R. Waser, I. B. Misirlioglu, S. P. Alpay and R. Ramesh, Appl. Phys. Lett. 86, 192910 (2004).
15. Y. L. Li, S. Y. Hu, S. Choudhury, M. I. Baskes, A. Saxena, T. Lookman, Q. X. Jia, D. G. Schlom and L. Q. Chen, J. Appl. Phys. 104, 104110 (2008).
16. Y. Wang, M. K. Niranjan, K. Janicka, J. P. Velev, M. Ye. Zhuravlev, S. S. Jaswal, and E. Y. Tsymbal, Phys. Rev. B **82**, 094114 (2010).
17. Y. Xiao, V. B. Shenoy and K. Bhattacharya, Phys. Rev. Lett. **95**, 247603 (2005).
18. Y. Zhang, J. Li, and D. Fang, Phys. Rev. B **82**, 064103 (2010).
19. L. Hong, A. K. Soh, Q. G. Du and J. Y. Li, Phys. Rev. B **77**, 094104 (2008).
20. B. Xu, L. E. Cross and J. J. Bernstein, Thin Solid Films **377-378**, 712 (2000).
21. J. H. Haeni, P. Irvin, W. Chang, R. Uecker, P. Reiche, Y. L. Li, S. Choudhury, W. Tian, M. E. Hawley, B. Craigo, A. K. Tagantsev, X. Q. Pan, S. K. Streiffer, L. Q. Chen, S. W. Kirchoefer, J. Levy and D. G. Schlom, Nature **430**, 758 (2004).
22. K. Dayal and K. Bhattacharya, Acta Mat. **55**, 1907 (2007).
23. B. Xu, R. G. Polcawich, S. Troiler-McKinstry, Y. Ye and L. E. Cross, Appl. Phys. Lett. **75**, 4180 (1999).
24. M. Y. El-Naggar, K. Dayal, D. G. Goodwin, and K. Bhattacharya, J. Appl. Phys. **100**, 114115 (2006).
25. K. Torii, E. L. Colla, H. W. Song, A. K. Tagantsev, K. No and N. Setter, Integ. Ferro. 32, 907 (2001).

26. Q. Zhou, Q. Zhang, B. Xu and S. Troiler-Mckinstry, J. Am. Cer. Soc. **85**, 1997 (2002).

27. T. V. Rivkin, C. M. Carlson, P. A. Parilla, D. S. Ginley, Integ. Ferro. 29, 215 (2000).

28. N. A. Pertsev, A. G. Zembilgotov and A. K. Tagantsev, Phys. Rev. Lett. **80**, 1988 (1998).

29. A. P. Levanyuk and A. S. Sigov, "*Defects and Structural Phase Transitions*", Volume 6, in *Ferroelectricity and Related Phenomena*, edited by W. Taylor, Gordon and Breach Science Publishers, (1988).

30. S. Pöykkö and D. J. Chadi, Phys. Rev. Lett. **83**, 1231 (1999).

31. E. Cockayne and B. P. Burton, Phys. Rev. B **69**, 144116 (2004).

32. A. M. Bratkovsky and A. P. Levanyuk, Phys. Rev. B **61**, 15042 (2000).

33. A. N. Morozovska and E. A. Eliseev, J. Phys.: Cond. Mat. **16**, 8937 (2004).

34. L. Pintilie and M. Alexe, J. Appl. Phys. **98**, 123103 (2005).

35. P. Zubko, D. J. Jung, and J. F. Scott, J. Appl. Phys. **100**, 114112 (2006).

36. I. B. Misirlioglu, M. Alexe, L. Pintilie and D. Hesse, Appl. Phys. Lett. **91**, 022911 (2007).

37. M. B. Okatan and S. P. Alpay, Appl. Phys. Lett. 95, 092902 (2009).

38. M. B. Okatan, J. V. Mantese and S. P. Alpay, Acta Mat. 58, 39 (2010).

39. V. Anbusathaiah, V. Nagarajan and S. Aggarwal, Appl. Phys. Lett. 89, 132912 (2006).

Figure Captions:

Figure 1. (Color online) (a) A schematic of the finger electrode capacitor. The potential in (b) and the in-plane polarization components in (c) are shown for demonstrative purposes.

Figure 2. (Color online) The *p*-type defects in this study. The dashed circle in the middle denotes the missing oxygen ion while the red atoms denote the Ti ions. The arrows indicate the shift of the positively charged Ti ions, forming a antiparallel configured dipole couple of not-ferroelectric origin. 1 and 2 denote the possible configurations considered in this work.

Figure 3. (Color online) Map of P_x in (a) 8 nm thick defect-free IFEC film under bias, (b) 8 nm thick defect-free IFEC film after bias removed, (c) 16 nm thick defect-free IFEC film under bias, (d) 16 nm thick defect-free IFEC film after bias removed.

Figure 4. (Color online) Map of P_x in (a) 8 nm thick IFEC film with *p*-type defects under bias, (b) 8 nm thick IFEC film with *p*-type defects after bias removed.

Figure 5. (Color online) Map of P_x in (a) 16 nm thick IFEC film with *p*-type defects under bias, (b) 16 nm thick IFEC film with *p*-type defects after bias removed.

Figure 6. (Color online) Map of P_x in (a) 16 nm thick IFEC film with homogeneous space charge density of 10^{26} C/m^3 under 4V bias and (b) after bias removed, (c) P_x in 8 nm thick IFEC film with homogeneous space charge density of 10^{26} C/m^3 under bias and (d) after bias removed.

Figure 7. (Color online) Hysteresis loops and dielectric displacement along *z* (right axis) for defect-free (a) 8 nm thick IFEC film and (b) 16 nm thick IFEC film. 'BE' (b) stands

for ‘bottom electrode’ and the green curve is provided to display the dielectric displacement at the surface between the electrodes when there is no bottom electrode.

Figure 8. (Color online) Hysteresis loops and displacement along *z* (right axis) for (a) 8 nm thick IFEC film and (b) 16 nm thick IFEC film with polar *p*-type defects.